Application of Cu_xO-Fe_yO_z Nanocatalysts in Ethynylation of Formaldehyde

Haitao Li *[ORCID]**, Lijun Ban, Zhuzhu Niu, Xin Huang, Pingfan Meng, Xudong Han, Yin Zhang, Hongxi Zhang and Yongxiang Zhao ***

Engineering Research Center of Ministry of Education for Fine Chemicals, School of Chemistry and Chemical Engineering, Shanxi University, Taiyuan 030006, China; banlijun1992@163.com (L.B.); niuzhuzhu163@163.com (Z.N.); hx06592661@163.com (X.H.); mpf15091823973@163.com (P.M.); hxd5609@163.com (X.H.); sxuzhy@sxu.edu.cn (Y.Z.); zhanghx@163.com (H.Z.)
* Correspondence: htli@sxu.edu.cn (H.L.); yxzhao@sxu.edu.cn (Y.Z.); Tel.: +86-138-3457-8761 (H.L.)

check for updates

Abstract: Composite nanomaterials have been widely used in catalysis because of their attractive properties and various functions. Among them, the preparation of composite nanomaterials by redox has attracted much attention. In this work, pure Cu_2O was prepared by liquid phase reduction with $Cu(NO_3)_2$ as the copper source, NaOH as a precipitator, and sodium ascorbate as the reductant. With $Fe(NO_3)_3$ as the iron source and solid-state phase reaction between Fe^{3+} and Cu_2O, Cu_xO-Fe_yO_z nanocatalysts with different Fe/Cu ratios were prepared. The effects of the Fe/Cu ratio on the structure of Cu_xO-Fe_yO_z nanocatalysts were studied by means of X-ray diffraction (XRD), Fourier transform infrared spectroscopy (FTIR), ultraviolet confocal Raman (Raman), scanning electron microscopy (SEM), X-ray photoelectron spectroscopy (XPS, XAES), and hydrogen temperature-programmed reduction (H_2-TPR). Furthermore, the structure–activity relationship between the structure of Cu_xO-Fe_yO_z nanocatalysts and the performance of formaldehyde ethynylation was discussed. The results show that Fe^{3+} deposited preferentially on the edges and corners of the Cu_2O surface, and a redox reaction between Fe^{3+} and Cu^+ occurred, forming Cu_xO-Fe_yO_z nanoparticles containing Cu^+, Cu^{2+}, Fe^{2+}, and Fe^{3+}. With the increase of the Fe/Cu ratio, the content of Cu_xO-Fe_yO_z increased. When the Fe/Cu ratio reached 0.8, a core–shell structure with Cu_2O inside and a Cu_xO-Fe_yO_z coating on the outside was formed. Because of the large physical surface area and the heterogeneous structure formed by Cu_xO-Fe_yO_z, the formation of nonactive Cu metal is inhibited, and the most active species of Cu^+ are exposed on the surface, showing the best formaldehyde ethynylation activity.

Keywords: Cu_xO-Fe_yO_z complex; formaldehyde ethynylation; core–shell; 2-butyne-1,4-diol

1. Introduction

1,4-butynediol (BYD) is a kind of alkynediol compound with C≡C and OH groups. It has active chemical properties and can be widely used in electroplating solutions, artificial leathers, medicine, pesticides, and other fields [1–4]. BYD hydrogenation can produce 1,4-butanediol (BDO), 1,4-butenediol, and so on. Hydrogenation products can be further extended downstream to tetrahydrofuran (THF), gamma-butyrolactone (gamma-GBL), polyurethane (PU), polybutylene terephthalate (PBT), polybutylene succinate (PBS), and so on [3–6]. In recent years, with the rapid development of downstream polyester materials, pharmaceutical intermediates, and other industries, the quality and demand for 1,4-butynediol has increased year by year [7].

1,4-butanediol is synthesized from formaldehyde and acetylene by the Reppe method with copper-based catalysts in industry. The development of high-performance Cu-based ethynylation

catalysts has attracted much attention. From the perspective of carrier selection, Cu-based catalysts supported on diatomite, silica gel, activated carbon, and transition or hydrated Al_2O_3 and SiO_2-MgO complexes have been reported in the literature [8–12]. In recent years, we have studied the new CuO-Bi_2O_3/SiO_2-MgO aerogel catalyst, the magnetic separation CuO-Bi_2O_3/Fe_3O_4-SiO_2-MgO catalyst, and the core–shell structure CuO-Bi_2O_3@SiO_2 catalyst. The catalyst supported on TiO_2 showed better activity and stability in the formaldehyde ethynylation reaction [13–18].

Another widely used catalyst for formaldehyde ethynylation is nano-Cu-based powder catalysts without support (CuO or Cu_2O). In a slurry bed reactor, nano-Cu-based powder catalysts often show higher performances. It was found that the crystallinity of Cu_2O species could be well regulated by controlling the precipitation conditions and methods, and then Cu_2O could be efficiently converted into an active component, cuprous acetylide, in the formaldehyde ethynylation reaction, thus significantly improving the catalytic activity of the catalyst. Later research confirmed that the introduction of additives into CuO to prepare multicomponent composite nanocatalysts can not only improve the dispersion of copper species, but the additives can further improve the catalytic activity through electronic effects or synergistic adsorption. The introduction of Bi_2O_3 can effectively inhibit the excessive reduction of copper species to metal Cu^0 in the formaldehyde ethynylation reaction, which results in catalyst deactivation [17]. The introduction of MgO enhances the surface alkalinity of the catalyst. The synergistic effect of a Cu center and a base center promotes the activation and adsorption of acetylene, and it makes the catalyst show higher catalytic activity [19]. The activation and adsorption of formaldehyde molecules has been realized by introducing copper centers and zinc oxide. The ethynylation performance of formaldehyde has further improved [20].

As an n-type semiconductor, Fe_2O_3 has been widely used in the photocatalytic field. It has been found that introducing Fe_2O_3 into Cu_2O can form p–n heterostructures [21], which have strong interactions and transfer electrons between Cu species and Fe species, and helps to regulate the reducibility of Cu species. In the magnetically separated CuO-Bi_2O_3/Fe_3O_4-SiO_2-MgO catalysts prepared by Wang Junjun et al. [16], the introduction of Fe_3O_4 not only played a role in magnetic separation, but also affected the existence of Cu species through the effect of electronic promoters, which led to an excellent formaldehyde ethynylation performance. Fe is considered as a good additive for formaldehyde ethynylation. Fe^{2+} and Fe^{3+} are reducible and oxidative in Fe_3O_4, while Cu^{2+} is converted to Cu^+ under the reductive condition of formaldehyde ethynylation, and the formation of inactive over-reductive metal Cu products should be inhibited. Cu_xO-Fe_yO_z nanocatalysts containing Cu^+, Cu^{2+}, Fe^{2+}, and Fe^{3+} were prepared. The stability of the active sites of Cu^+ in a reducing atmosphere could be improved by using the electronic effects among species with different valences; thus, the activity and stability of the formaldehyde ethynylation reaction could be improved.

A variety of synthetic protocols in both aqueous and nonaqueous media have been developed for large-scale synthesis of composite nanostructure catalysts. Redox transformation reactions have shown great potential for the synthesis of hollow/porous metal oxide nanoframeworks, alloy nanostructures, and composite nanostructure catalysts [22–26]. Recently, Pal et al. [27] reported a systematic and delicate size- and shape-controlled synthesis of CuO-MnO_2 composite nanostructure catalysts from time-dependent redox transformation reactions between Cu_2O and $KMnO_4$. The composite nanostructure catalysts acted as efficient recyclable catalysts for nitroarene reduction in water at room temperature. Fe^{3+} is an oxidizing metal similar to $KMnO_4$. In this work, a series of Cu_xO-Fe_yO_z catalysts with different Fe/Cu ratios were prepared by the redox reaction between Cu_2O and Fe^{3+} using iron nitrate as the Fe^{3+} source. The formation mechanism of the catalysts and the effects of the Fe/Cu ratio on the structure, texture, valence state of Cu species, reduction performance, and ethynylation activity of the catalysts were studied.

2. Materials and Methods

2.1. Preperation of Catalysts

All chemical reagents, Cu(NO$_3$)$_2$·3H$_2$O(Macklin), Fe(NO$_3$)$_3$·9H$_2$O(Macklin), PEG-600(Macklin) and NaOH(Macklin), were of analytic grade and used as-purchased without pre-purification.

Cu$_2$O: 100 mL of 0.125 mol/L Cu(NO$_3$)$_2$·3H$_2$O solution was transferred into a 1000 mL beaker, and the beaker was placed in a constant temperature water bath at 30 °C. PEG-600 (100 mL) was added to the above solution under magnetic stirring. A total of 150 mL of 1.67 mol/L NaOH solution was measured and poured into the beaker. After magnetic stirring for 5 min, 300 mL of 0.25 mol/L sodium L-ascorbate solution was added dropwise, and the dropping rate was 1.25 mL/min. Then, the mixture was stirred continually for 30 min and was allowed to stand for 1 h at a constant temperature. After being centrifuged, the mixture was washed three times with distilled water and absolute ethanol, and it was dried in a vacuum dryer at 60 °C for 4 h. The obtained sample was marked as Cu$_2$O.

Cu$_x$O-Fe$_y$O$_z$: 2 g of the above prepared Cu$_2$O powder was dispersed in 10 mL of Fe(NO$_3$)$_3$·9H$_2$O aqueous solution. The solution was sonicated at room temperature for 20 min, magnetically stirred for 30 min, and centrifuged to obtain the solid material. The solid material was dried at 60 °C for 10 h in a vacuum dryer, and it was calcined at 300 °C for 3 h under a nitrogen atmosphere to form Cu$_x$O-Fe$_y$O$_z$. The concentrations of Fe(NO$_3$)$_3$·9H$_2$O aqueous solution in the above preparation procedure were adjusted to 0.01, 0.1, 1, and 2 mol/L, respectively, and a series of different Fe/Cu ratios of Cu$_x$O-Fe$_y$O$_z$ were synthesized. The Fe/Cu molar ratios of the five catalysts prepared at different concentrations were determined by inductively coupled plasma atomic emission spectroscopy (ICP) to be 0.05, 0.1, 0.8, and 2, respectively, and the samples were marked as CF-0.05, CF-0.1, CF-0.8, and CF-2.

2.2. Characterization of Catalysts

N$_2$-Physisorption analyses were performed using a Micromeritics ASAP-2020 apparatus (Norcross, GA, USA). The fresh and used samples were degassed at 150 °C for 5 h and 60 °C for 24 h, respectively, prior to adsorption testing. Specific surface areas were obtained using the multipoint Barrett-Emmett-Teller (BET) procedure.

X-ray diffraction patterns of the samples were recorded with a D8 Advance diffractometer (Bruker Corporation, Billerica, MA, USA) with Cu Kα radiation (λ = 1.5418 Å).

Fourier transform infrared (FTIR) spectra were recorded with a Nicolet™ iS50 spectrophotometer (Thermo Fisher Scientific, Waltham, MA, USA) in the range of 400–4000 cm^{-1}.

Scanning electron microscopy (SEM) images were obtained with Hitachi S4800 electron microscope operated at beam energy of 3.0 kV.

Raman spectroscopy was performed with a LabRAM HR Evolution Raman spectrograph (HORIBA Scientific, Paris, France) with a 532 nm laser operated at 0.08 mW.

X-ray photoelectron spectroscopic (XPS) measurements were conducted on an ESCALAB 250 spectrometer (Thermo Fisher Scientific, Waltham, MA, USA) using an Al Kα X-ray source (hν = 1486.7 eV).

Auger electron spectroscopy (XAES) was performed on a PHI 1600 ESCA spectrometer (Perkin-Elmer, Waltham, MA, USA) equipped with a monochromatic Al Ka X-ray source (hm = 1361 eV) operating at a pass energy of 100 eV.

H$_2$ temperature-programmed reduction (H$_2$-TPR) experiments were performed on a Micromeritics AutoChem II 2920 automatic temperature-programmed chemical adsorption instrument (Norcross, GA, USA), and about 30 mg of the sample was loaded into a quartz U-tube for each measurement. Prior to the measurement, the sample was treated at 350 °C for 2 h under Ar stream. When the temperature was dropped to 50 °C, the H$_2$-Ar mixture (5% H$_2$ by volume) was switched on, and the temperature increased with a ramp of 10 °C/min.

2.3. Catalyst Test of Catalysts

The catalyst was evaluated in a three-neck flask connected with a reflux condenser. A blend of a quantity of catalyst with 50 mL of formaldehyde (35 wt.%) aqueous solution was carried out in an oil-bath flask under electromagnetic stirring. An adequate quantity of pure N_2 was poured into the flask to purge O_2, and the solution containing the catalyst was heated to reaction temperature (90 °C) under continuous agitation. A C_2H_2 stream was then turned on to initiate the ethynylation reaction. After several hours, by lowering the reaction temperature to room temperature, the catalytic reaction was stopped, an N_2 stream was poured, and the C_2H_2 stream was shut down.

The used catalyst was centrifuged, washed in deionized water, and dried in a vacuum at ambient temperature. In the centrifugal solution, the formaldehyde content was titrated with sodium thiosulfite to get the conversion rate of formaldehyde. The analysis of 1,4-butynediol content on an Agilent 7890A gas chromatography (Santa Clara, CA, USA) was conducted using the internal standard method with the addition of 1,4-butanediol. The selectivity of 1,4-butynediol was obtained through the method of dividing the yield of 1,4-butynediol by the conversion rate of formaldehyde [7].

3. Results

3.1. Structure Analysis of Catalysts

The phase and composition of catalysts were characterized by X-ray diffractometry (XRD), and the obtained XRD patterns are shown in Figure 1. Peaks obtained in the XRD pattern confirmed the crystalline formation of Cu_2O. The sharp characteristic diffraction peaks at the 2θ angles of 29.6, 36.5, 42.4, 61.4, 73.6, and 77.4 can be indexed to (110), (111), (200), (220), (311), and (222) planes, respectively, of the cubic cuprous oxide phase (JCPDS card No. 05-0667) [28]. After loading of Fe during the reaction process, the intensity of the Cu_2O peaks became gradually weaker with the increase of the Fe/Cu weight ratio. The Cu_2O peaks in CF-2 almost disappeared. The diffused characteristic diffraction peaks located at the 2θ angles 35.5 and 38.7 can be assigned to the diffraction of Fe_2O_3 nanoparticles, indicating that the Cu_2O content decreased, and the dispersion increased. The loaded Fe_2O_3 existed in an amorphous or highly dispersed form. It is speculated that the loaded Fe species was not simply adsorbed on the Cu_2O surface, but it reacted with Cu_2O, causing a change in the state of Cu_2O itself.
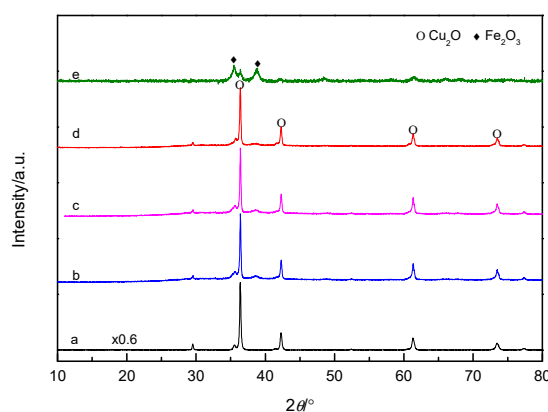

Figure 1. XRD patterns of Cu_2O and Cu_xO-Fe_yO_z with different Fe/Cu ratios (**a**) Cu_2O, (**b**) CF-0.05, (**c**) CF-0.1, (**d**) CF-0.8, and (**e**) CF-2.

3.2. FT-IR Analysis and Raman Analysis

Figure 2 represents the FT-IR spectrum of the Cu_2O and Cu_xO-Fe_yO_z catalysts with different Fe/Cu weight ratios. As shown in the infrared spectrum of Cu_2O, the infrared absorption peak observed at 622 cm^{-1} was assigned to Cu(I)–O bond stretching and bending vibration modes [29]. After loading of Fe, the absorption peaks centered at 475 cm^{-1} and 552 cm^{-1} were assigned to the Fe^{3+}–O^{2-} bond stretching in the FeO_6 octahedron and Fe^{3+}–O^{2-} bond stretching in the FeO_4

tetrahedron, respectively [30]. The infrared absorption peak of Cu_2O observed at 622 cm^{-1} became weaker with the increase of Fe/Cu weight ratio; the peak almost disappeared when the Fe/Cu weight ratio was 2, indicating the decrease of relative content of Cu_2O or the conversion of species.
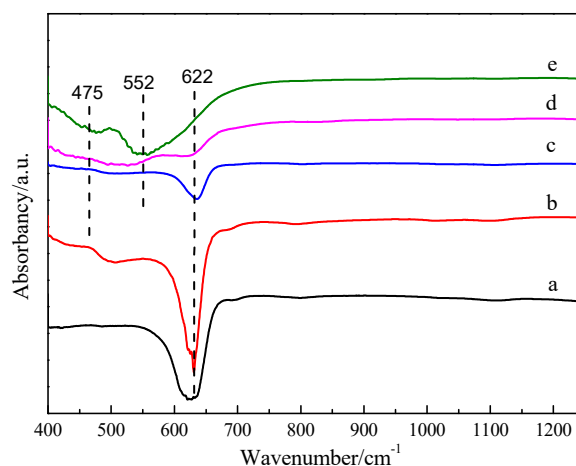

Figure 2. FT-IR spectra of Cu_2O and Cu_xO-Fe_yO_z with different Fe/Cu ratios (**a**) Cu_2O, (**b**) CF-0.05, (**c**) CF-0.1, (**d**) CF-0.8, and (**e**) CF-2.

Raman spectroscopy has been widely used to characterize crystal structures and for qualitative analysis. Cu_2O has a simple cubic lattice and belongs to the O_{4h} space group [31]. According to the space group theory, Cu_2O has six vibration modes, $\Gamma = F_{2g} + 2F_{1u} + F_{2u} + E_u + A_{2u}$. Theoretically, for a perfect Cu_2O crystal, only the F_{2g} vibration mode has Raman activity, and the two F_{1u} vibration modes have infrared activity. However, due to the lattice defects, not only the intensity of the intrinsic peaks is reduced or even masked, but also the vibrational modes of non-Raman activity are excited. These have become an important basis for identifying Cu_2O species [32,33]. Figure 3 is a Raman spectrum of the catalyst. The characteristic Raman shifts of the Cu_2O catalyst can be observed at 148, 218, 414, 520, and 631 cm^{-1}. According to the literature, the observed Raman peaks can be assigned to the F2g vibration mode at 520 cm^{-1}, the infrared active F1u vibration modes at 148 and 631 cm^{-1}, and the multiphonon vibration modes at 218 and 414 cm^{-1}. With the increase of the Fe/Cu weight ratio, the intensity of the Raman vibration peak of Cu_2O at 218 cm^{-1} decreased, and it even disappeared when Fe/Cu was 0.8. At the same time, the diffused Raman shift assigned to the Fe_2O_3 species can be observed at 248 and 720 cm^{-1} [34,35]. This indicates that the initial loaded low content of Fe led to a decrease in the crystallinity of the Cu_2O surface, and the loading of a large amount of Fe_2O_3 made the surface of Cu_2O highly dispersed or covered by Fe_2O_3. Comparing the XRD spectrum with the Raman spectrum of the CF-0.8 sample whose Fe/Cu ratio was 0.8, it can be found that a clear crystal diffraction peak assigned to Cu_2O was still observed in XRD, and in the Raman spectrum, the characteristic Raman shift assigned to Cu_2O disappeared. Considering that the XRD spectrum depicts phase characteristics, while the Raman spectra gives the characteristics of the surface information of the sample, it can be speculated that CF-0.8 formed the amorphous Cu-Fe composite at the surface, and the interior was still a covering structure of the Cu_2O crystal. Comparing the XRD with Raman characterization data of each sample with the increase of the Fe/Cu ratio, it is further speculated that there was a reaction between Fe^{3+} and Cu^+, and the reaction gradually expanded from the surface of Cu_2O to the bulk phase until complete conversion.
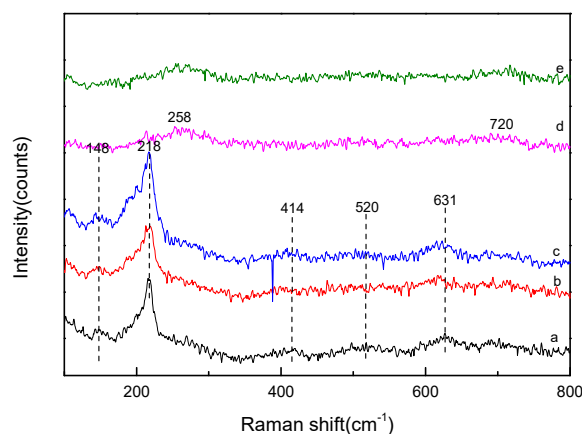
Figure 3. Raman spectra of Cu_2O and Cu_xO-Fe_yO_z with different Fe/Cu ratios (**a**) Cu_2O, (**b**) CF-0.05, (**c**) CF-0.1, (**d**) CF-0.8, and (**e**) CF-2.

3.3. Morphological Analysis

To observe whether Fe-doping had an impact on the surface structure, crystal phase, and chemical composition of the catalyst, the catalyst was characterized by SEM, and an EDS element analysis was carried out on the selection. The results are shown in Figure 4 and Table 1. Figure 4a is an SEM image of Cu_2O. It can be observed that the pure Cu_2O crystal had an octahedral morphology [36], and the particles were intact and uniform in size. According to the EDS analyses of the selected crystal plane a1 and the vertex corner a2, it was discovered that only the Cu element exists (Table 1). After Fe was introduced into Cu_2O, and when the Fe/Cu ratio was 0.05, it was found that irregular particles were attached at the edges, arrises, and corners of the Cu_2O crystal, and the Cu_2O crystal plane maintained the original features. According to the respective EDS analyses of the selected newly formed, irregular particles b1 and Cu_2O crystal plane b2, it was shown that only Cu existed in the b2 area, and both Fe and Cu elements existed in the b1 area. When the Fe/Cu ratio reached 0.1, the irregular particles in the CF-0.1 sample increased, while the Cu_2O crystal plane decreased. The proportion of irregular particles increased from 13.8% to 21.9% with an Fe/Cu ratio of 0.05. This result indicated that when Fe^{3+} was introduced into Cu_2O, the irregular particles formed were not the physical adhesion of the formed Fe_2O_3, but the nanoparticles were formed by the reaction between Cu_2O and Fe^{3+}. Since the edges, arrises, and corners of the Cu_2O crystal are at a high energy, the composite nanoparticles are preferentially formed here, and as the Fe/Cu ratio increased, the exposed Cu_2O crystal plane decreased. The exposed Cu_2O crystal plane still existed in the SEM image of the CF-0.1 sample, which corresponds to the obvious Cu_2O characteristic peak in the XRD and Raman spectra. When the Fe/Cu ratio was increased to 0.8, it was discovered in the CF-0.8 sample that the surface of the Cu_2O crystal was completely destroyed, and the overall surface showed a rough spherical morphology. After EDS tests, the surface chemical composition was evenly distributed, and the Fe/Cu ratio in different areas was 1 (or so). Combined with XRD and Raman characterizations, the XRD spectrum of Cu_2O could still be observed in the CF-0.8 sample, while the Raman shifts disappeared, indicating that the core–shell structure with an inner core of Cu_2O and an outer shell of Fe-Cu composite formed. By further increasing the Fe/Cu ratio, a rough, spherical morphology can be observed in the CF-2 sample, and Cu_2O reacted completely with the introduced Fe to form a phase Fe-Cu composite.

Table 1. EDS element analysis of different regions.

Catalysts	Region	AT%		
		OK	FeK	CuK
Cu_2O	a1	7.67	0	92.33
	a2	8.97	0	91.03

Table 1. *Cont.*

Catalysts	Region	AT%		
		OK	FeK	CuK
CF-0.05	b1	7.85	0	92.15
	b2	13.91	10.46	75.63
CF-0.1	c1	8.67	0	91.33
	c2	17.36	14.84	67.80
CF-0.8	d1	29.33	35.74	34.92
	d2	29.12	35.97	34.91
CF-2	e1	33.23	41.96	24.81
	e2	34.12	41.72	24.16
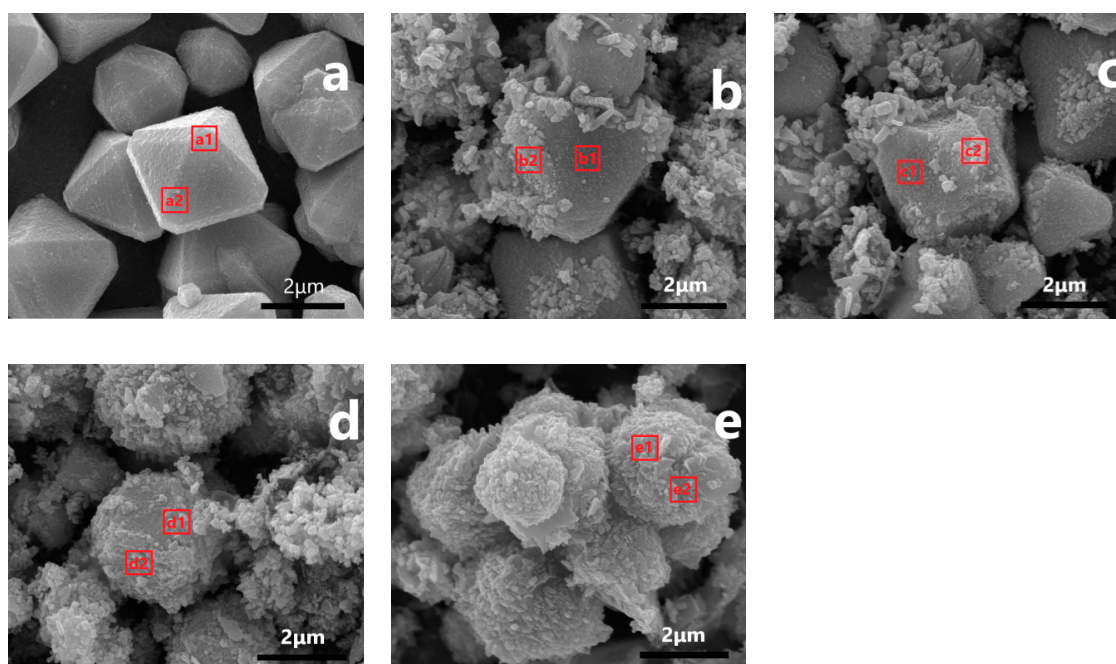
Figure 4. SEM images of Cu_2O and Cu_xO-Fe_yO_z with different Fe/Cu ratios (**a**) Cu_2O, (**b**) CF-0.05, (**c**) CF-0.1, (**d**) CF-0.8, and (**e**) CF-2.

3.4. Surface Composition and Valence Analysis of the Catalyst

XPS characterization is widely used in catalyst material analysis. To determine the composition of samples with different Fe/Cu ratios, XPS usually has a certain degree of transparency to the surface, and the Cu-O system can reach 9–10 monolayers.

The Cu2p images of Cu_2O, CF-0.8, and CF-2 were selected for peak fitting, and the peak positions and surface atomic ratios of different valence elements were calculated according to the fitting images, which are shown in Figure 5 and Table 2. It can be seen from the data of the peak fitting that Cu_2O, CF-0.8, and CF-2 had two XPS characteristic peaks at 932.5 and 952.4 eV, which correspond to the binding energies of $Cu2p_{3/2}$ and $Cu2p_{1/2}$ in Cu_2O. Two XPS characteristic peaks also appeared at higher binding energies (934.5 and 954.6 eV), corresponding to $Cu\,2p_{3/2}$ and $Cu\,2p_{1/2}$ in CuO, respectively [37,38]. In addition, the 2p → 3d satellite peak of Cu^{2+} appeared at 941–945 eV, further confirming the presence of CuO species on the surface of the sample. According to the corresponding integral data of the Cu^{2+}→Cu^{+} peak area at $Cu2p_{3/2}$, the atomic ratios of Cu^{2+}/Cu^{+} on different samples were calculated (Table 2). It can be seen that there was also Cu^{2+} in pure CuO, and the ratio of Cu^{2+}/Cu^{+} was 0.31, which may be due to the oxidation of partial Cu_2O surface by O_2 to CuO during sample preparation. With the increase of Fe content, the ratio of Cu^{2+}/Cu^{+} on the surface of the catalyst

increased, and the ratio of Cu^{2+}/Cu^+ in CF-2 reached 2.3, indicating that more CuO formed. At the same time, it was found that in CF-0.8 and CF-2 prepared by introducing Fe, the binding energy at $Cu2p_{3/2}$ corresponding to Cu^+ shifted to a high binding energy of 932.8 eV.

According to the peak fitting for the Fe2p XPS images of CF-0.05, CF-0.8, and CF-2 catalysts, it can be seen that all catalysts had two XPS characteristic peaks at 711.6 and 725.5 eV, corresponding to the binding energies of $Fe^{3+}2p_{3/2}$ and $Fe^{3+}2p_{1/2}$ in Fe_2O_3 [39], indicating that most of the Fe species in the prepared catalysts existed in the form of Fe^{3+}. Two XPS characteristic peaks also appeared at 710.1 and 724 eV, corresponding to the binding energies of $Fe^{2+}2p_{3/2}$ and $Fe^{2+}2p_{1/2}$ [40]. The Fe^{2+}/Fe^{3+} atomic ratio data calculated from the peak areas of Fe^{2+} and Fe^{3+} at the $Fe2p_{3/2}$ peak are listed in Table 2. It can be seen that the surface Fe^{2+}/Fe^{3+} ratio increased with the increase of the Fe/Cu ratio because more Fe^{3+} was converted to Fe^{2+} in the reaction process. In Figure S1, it is shown that as the Fe/Cu ratio was lower than 0.8, the peak area of Fe2p increased with the increase of the Fe/Cu ratio, which was attributed to the enrichment of Fe on the surface of the catalyst particles. When the Fe/Cu ratio was further increased by 2, the peak area of Fe2p decreased. In response to this phenomenon, we analyzed the O/Fe+Cu+O ratio on each sample, and the results are listed in supporting information (Table S1). Table S1 shows that the ratio of O/Fe+Cu+O increased with the increase of the Fe/Cu ratio. We speculate that the Fe2p integrated area of CF-2 decreased because of the increased O content. The increase of O content in the surface was due to the conversion of Cu_2O to CuO and the increase of O atoms bound to Fe^{3+}. Synthesized with the results of the increase of Cu^{2+}/Cu^+ and Fe^{2+}/Fe^{3+} ratios in the sample introduced into Fe, it is speculated that a redox reaction occurred between Cu_2O and Fe^{3+}, and a Cu_xO-Fe_yO_z shell formed on the outer surface of Cu_2O. In addition, after the introduction of Fe, the Cu^+ electron binding energy increased. It was also indicated that a heterostructure formed between Cu_xO-Fe_yO_z, which decreased the density of the Cu^+ electron cloud and increased the binding energy of the Cu^+ electron cloud.
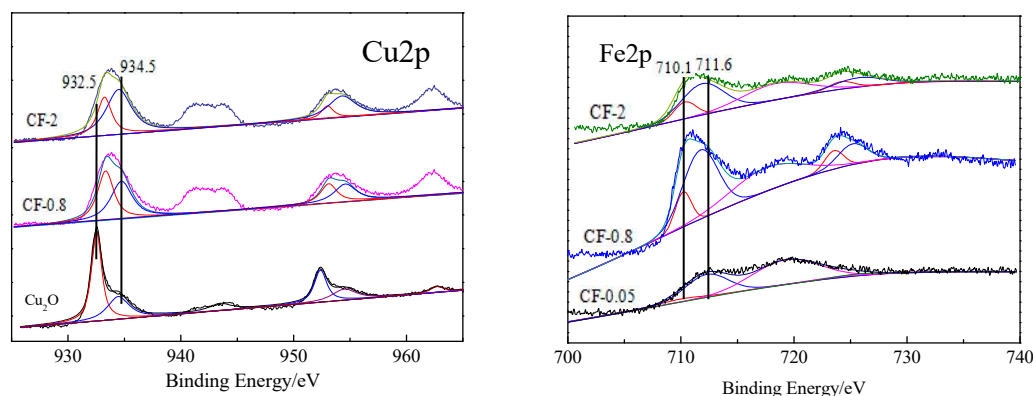

Figure 5. XPS spectra of Cu_2O and Cu_xO-Fe_yO_z.

Table 2. Peak position and peak area ratio of different elements and valence states.

Catalysts	Fe(eV)		Fe^{2+}/Fe^{3+} (Atomic)	Cu(eV)		Cu^{2+}/Cu^+ (Atomic)	Fe/Cu (Atomic)
	$Fe^{2+}2p_{3/2}$	$Fe^{3+}2p_{3/2}$		$Cu^+2p_{3/2}$	$Cu^{2+}2p_{3/2}$		
Cu_2O	-	-	-	932.4	934.7	0.31	-
CF-0.05	710.1	711.6	0.07	-	-	-	0.26
CF-0.8	710.1	711.6	0.26	932.8	934.7	0.83	0.79
CF-2	710.1	711.6	0.32	932.8	934.7	2.3	1.23

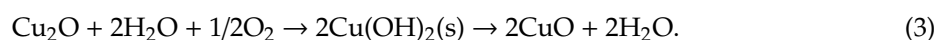### 3.5. Discussion on the Formation Mechanism of Cu_xO-Fe_yO_z Structure

By virtue of the redox reaction between Cu_2O and Fe^{3+}, Cu_xO-Fe_yO_z can be prepared by controlling the concentration of the initial Fe^{3+}. The synthesis and morphology control of Cu_2O has been fully discussed in the literature and is not discussed in this work [41–44]. When the concentration of the

initial $Fe(NO_3)_3 \cdot 9H_2O$ solution was 0.8 mol/L, the prepared catalyst exhibited a core–shell structure, where the inner layer was Cu_2O and the outer layer was coated with $Cu_xO\text{-}Fe_yO_z$ (Figure 4d). Based on the XPS analysis of the sample, the outer structure contained two metal elements, Fe and Cu. Fe presents two valence states of Fe^{2+} and Fe^{3+}, while Cu exhibits valence states of Cu^{2+} and Cu^+ (Figure 5). In the initially prepared Cu_2O, there were also CuO species derived from the oxidation of O_2 during the preparation procedures, and the CuO species increased significantly after Fe^{3+} treatment. At the same time, under the condition of nonisolating O_2, the reduced state product Fe^{2+} of Fe^{3+} was produced, which was inevitably derived from the reduction of Cu^+. The standard reduction potential of Fe^{3+}/Fe^{2+} was 0.771V, while the standard reduction potential of Cu^{2+}/Cu^+ was +0.203 V. From the perspective of thermodynamics, the processes of oxidizing Cu^+ to Cu^{2+} by Fe^{3+} and converting Fe^{3+} itself into Fe^{2+} can be spontaneously carried out:

$$Fe^{3+} + Cu^+ \rightarrow Fe^{2+} + Cu^{2+}. \tag{1}$$

In the presence of water, it can be written in steps:

$$Fe^{3+} + 2OH^- + e^- \rightarrow Fe(OH)_2(s) \rightarrow FeO + H_2O; \tag{2}$$

$$Cu_2O + 2H_2O + 1/2 O_2 \rightarrow 2Cu(OH)_2(s) \rightarrow 2CuO + 2H_2O. \tag{3}$$

Cu^+ is oxidized to Cu^{2+}, and Fe^{3+} is converted to Fe^{2+} under the condition of nonisolating O_2, but these redox reactions selected in this work cannot be completely carried out. In the outer surface composition of the samples with an Fe/Cu ratio of 0.8 and Fe/Cu ratio of 2, Cu^+, Cu^{2+}, Fe^{3+}, and Fe^{2+} exist simultaneously, indicating that a redox balance was reached between them. And under such balance, it is difficult to further reduce Cu^+ and Cu^{2+} to a lower valence state and to oxidize Fe^{2+} to a higher valence state. Under the atmosphere of oxidizing O_2, oxides of different valence states can stably exist, and it is speculated that this composition exhibits good stability under a reducing atmosphere. By comparing the SEM results of $Cu_xO\text{-}Fe_yO_z$ prepared by different concentrations of $Fe(NO_3)_3$ solution, it was also found that the redox reaction between Cu_2O and Fe^{3+} went through the reaction process from the edge/arris/corner to the exposed surface and, finally, to the surface phase. The driving force for nucleation results from the difference of surface free energy [45,46]. Exposed high refractive index surfaces, defects, atomic steps, and kinks can be used as nucleation sites. The edge and vertex of Cu_2O have higher surface free energy than those of the crystal mask, so it can be preferentially used as nucleation site [47]. At low Fe^{3+} concentrations, Fe^{3+} preferentially reacts with Cu^+ at the edge, arris, and corner of the Cu_2O crystal to form amorphous $Cu_xO\text{-}Fe_yO_z$ particles, which partially cover only the position of the edge, arris, and corner of Cu_2O. In the regular Cu_2O crystal, the edge, arris, and corner are often distributed with more defects and are at higher energy levels, which are the main reason for the preferential oxidation-reduction between Cu_2O and Fe^{3+}.

With the increase of Fe^{3+} concentration, Cu_2O on the exposed crystal surface reacted with Fe^{3+}. When the concentration of Fe^{3+} was 0.8, Cu_2O converted into an amorphous sphere with a rough surface. XRD showed that its phase structure was still Cu_2O with complete crystal form, namely, forming the core–shell structure of $Cu_xO\text{-}Fe_yO_z$. When the Fe^{3+} concentration continued to increase, the excess Fe^{3+} concentration migrated to the phase through the amorphous shell and reacted with the phase Cu_2O to form a new $Cu_xO\text{-}Fe_yO_z$ complex, until the Cu_2O was destroyed as a whole, forming an amorphous $Cu_xO\text{-}Fe_yO_z$ and also causing changes in the texture–structural parameters of the catalyst. It can be seen from Table S2 that as the ratio of Fe/Cu increased, the specific surface area and pore volume first increased and then decreased (Figure 6).
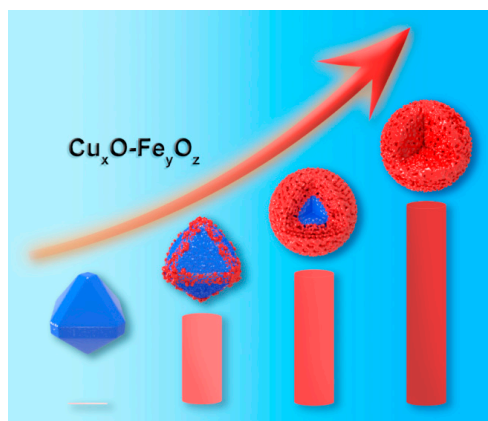
Figure 6. Formation of the Cu_xO-Fe_yO_z structure.

3.6. Analysis of Reduction Behavior of the Catalyst

The redox performance of the catalyst is one of the important factors affecting the activity of the catalyst. Cu_xO-Fe_yO_z catalysts with different Fe/Cu ratios were characterized by TPR. As can be seen from the Figure 7, the Cu_2O catalyst had a broad reduction peak in the range of 200 to 300 °C, and the peak temperature was 285 °C. After doping Fe, it was found that when the Fe content was less than 0.8, the reduction peak shapes of each catalyst were similar to that of the Cu_2O catalyst, and the peak temperature moved to a high-temperature range with the increase of Fe/Cu ratio. The peak temperatures in CF-0.05, CF-0.1, and CF-0.8 were 297, 305, and 325 °C, respectively. These indicate that the doping of Fe did not destroy the crystal phase structure of Cu_2O, and the reduction peak was the hydrogen-consuming peak of Cu metal reduced from Cu_2O. The start/stop reduction temperature of the catalyst shifted to the direction of high temperature, revealing that there was a certain interaction in the catalyst, and the corresponding copper-iron heterostructure formed to reduce the reduction of Cu_2O. Combined with XPS analysis, the peak area of Fe2p increased with the increase of the Fe/Cu ratio (Figure S1). When CF-0.8 reached the maximum, it was shown that the enrichment of Fe on the surface of CF-0.8 reached the maximum, and a strong interaction between copper-iron complexes formed, which led to the highest reduction temperature. Compared with the Cu_2O catalyst, when the Fe/Cu ratio reached 2, the reduction peak had a large shift to the direction of low temperature. The peak temperature was 238 °C, and the peak shape was irregular. It is speculated from the results of XPS analysis that, perhaps because of the increase of Fe content, the crystal structure of Cu_2O was destroyed to form the isolated Cu^{2+} and Fe-Cu^+ and make the reduction peak shift to the direction of low temperature.
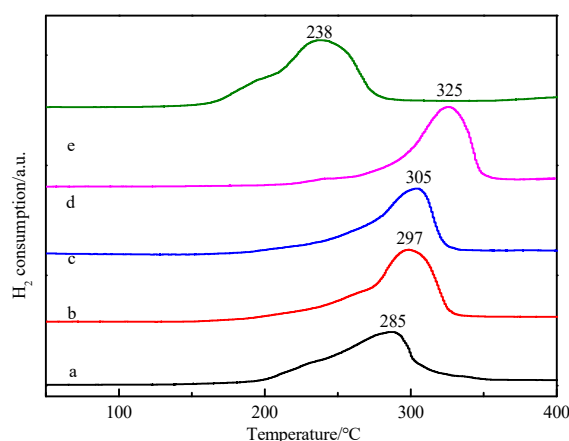

Figure 7. Temperature-programmed reduction (TPR) profiles of Cu_2O and Cu_xO-Fe_yO_z with different Fe/Cu ratios (**a**) Cu_2O, (**b**) CF-0.05, (**c**) CF-0.1, (**d**) CF-0.8, and (**e**) CF-2.

3.7. Evaluation Results of Catalyst Activity

The reaction of formaldehyde with acetylene can produce 2-propyn-1-ol and 2-butyne-1,4-diol: $HC \equiv CH + HCHO \rightarrow HC \equiv CCH_2\text{-}OH \rightarrow HO\text{-}CH_2C \equiv CCH_2\text{-}OH$. Theoretically, the solubility of C_2H_2 gas in HCHO solution is relatively low. In the aqueous phase reaction system, the concentration of HCHO is much larger than that of C_2H_2. In the reaction, it is easier for one molecule of acetylene to react with two molecules of formaldehyde to obtain BYD. The formation of propynyl alcohol is often required to be carried out at a high acetylene pressure and in a benign solvent such as γ-butyrolactone (GBL) and N-methylpyrrolidone (NMP). The system with acetylene gas in the atmospheric pressure and aqueous formaldehyde solution used in this work only produced BYD, and no formation of propynyl alcohol was observed. The yield of BYD in the reaction system directly reflects the activity of the catalyst. Figure 8a shows the BYD yield of Cu_2O and $Cu_xO\text{-}Fe_yO_z$ with different ratios. It can be seen that the yield of 2-butyne-1,4-diol in pure Cu_2O sample was only 21.8%. With the doping of Fe, the yield of 2-butyne-1,4-diol first increased and then decreased. The yield of 2-butyne-1,4-diol in the CF-0.8 sample reached a maximum of 59.83%, and CF-0.8 showed the best catalytic performance. The stability of two catalysts, Cu_2O and CF-0.8, was investigated. The results are shown in Figure 8b. It can be seen that the yield of 2-butyne-1,4-diol decreased in both catalysts during the 6-cycle test. But the decrease trends were significantly different: the yield of 2-butyne-1,4-diol on the Cu_2O catalyst decreased from about 22% to about 10%, while the yield of 2-butyne-1,4-diol in the CF-0.8 catalyst decreased from about 60% to about 50%. And in the second cycle test of the Cu_2O catalyst, the yield of 2-butyne-1,4-diol decreased significantly, while in the CF-0.8 catalyst, the yield of 2-butyne-1,4-diol decreased in the fourth cycle test, indicating that the CF-0.8 catalyst had a higher stability than the Cu_2O catalyst. By comparing with different catalysts (Table S3), it was found that the doping of Fe improved the catalytic activity, and the stability of the catalyst, which shows the advantages of $Cu_xO\text{-}Fe_yO_z$.

In ethynylation of formaldehyde, the initial Cu species (Cu^{2+} or Cu^+) in situ can be converted into the active species of the cuprous acetylide to exhibit catalytic activity. The Cu^+ site exposed on the surface of the catalyst after the reaction was positively correlated with the ethynylation activity of formaldehyde (i.e., BYD yield). In the $Cu_xO\text{-}Fe_yO_z$ catalyst system, exposure of the Cu^+ site on the surface of the catalyst after activation was determined by the following factors: (1) physical specific surface area of the catalyst, (2) Fe/Cu ratio on the surface of the catalyst, and (3) whether Cu^{2+} or Cu^+ was excessively reduced to inactive species of metal Cu. Combined with catalyst characterization, it was found that with the introduction of Fe species, the catalyst changed from a regular crystal structure to a coarse, amorphous structure. During this process, the specific surface area and pore volume increased significantly. The large specific surface area is favorable for the exposure of active species, the large pore structure is favorable for the diffusion of reactants and products, and it is advantageous for the improvement of catalytic activity. An unfavorable factor accompanying the change in specific surface is that Fe occupies part of the Cu site, which is not conducive to the exposure of Cu species, and the two factors mutually restrict each other. The specific surface areas and Fe/Cu ratios of the different samples are listed in Tables S1 and S2. It can be seen that the specific surface area of Cu_2O was only 7.7 m^2/g. After the introduction of Fe, the specific surface area of the sample notably increased. The specific surface area of the CF-0.8 sample reached 13.9 m^2/g, about twice that of Cu_2O. At this time, the surface Fe/Cu ratio was 0.79, and the amount of Cu exposed on the surface increased as a whole. When the Fe/Cu ratio further increased, the CF-2 specific surface area further increased to 17.6 m^2/g. However, it was difficult to compensate for the decrease of surface Cu species because of the increase of the Fe/Cu ratio. This is an important reason for the first increase and then decrease of BYD yield with an increasing Fe/Cu ratio.

On the other hand, it is worth noting that the above-discussed Cu species on the specific surface area contain various Cu species, including the Cu+ species in the active cuprous acetylide converted by ethynylation of formaldehyde and the inactive metal Cu species produced by over-reduction. The inactive metal Cu not only covered the effective active Cu^+ species but also decreased the active

Cu^+ species. Metallic Cu can catalyze the polymerization of acetylene, resulting in deactivation of carbon deposits on the catalyst surface. Under the premise of increasing the surface Cu species, regulating the chemical environment and reducibility of Cu species and preventing the production of over-reduced species Cu are the important factors to improve the performance of the ethynylation of formaldehyde for the catalyst. In the catalyst of Cu_xO-Fe_yO_z prepared by introducing Fe into Cu_2O, by virtue of the heterostructure formed between Cu_xO and Fe_yO_z, the electron cloud density of the Cu species was redistributed, a good stability in the redox atmosphere was maintained, and the Cu^+ species in the ethynylation of formaldehyde existed stably (Figure 5) to restrict the excessive reduction of Cu^+ to metallic Cu, which is another important factor that the CF-0.8 sample containing Fe had the highest ethynylation activity of formaldehyde. Figure 6 TPR confirmed that the introduction of a proper amount of Fe could regulate the reduction performance of Cu^+. In the sample after reaction, the XRD peak of metallic Cu appeared in Cu_2O, and the peak intensity of metallic Cu decreased with the increase of Fe/Cu ratio (Figure S3). The Auger electron spectroscopy after the reaction also showed that the peak area of the metal Cu in the Fe-containing sample decreased significantly (Figure S4). These results confirm the above inference.
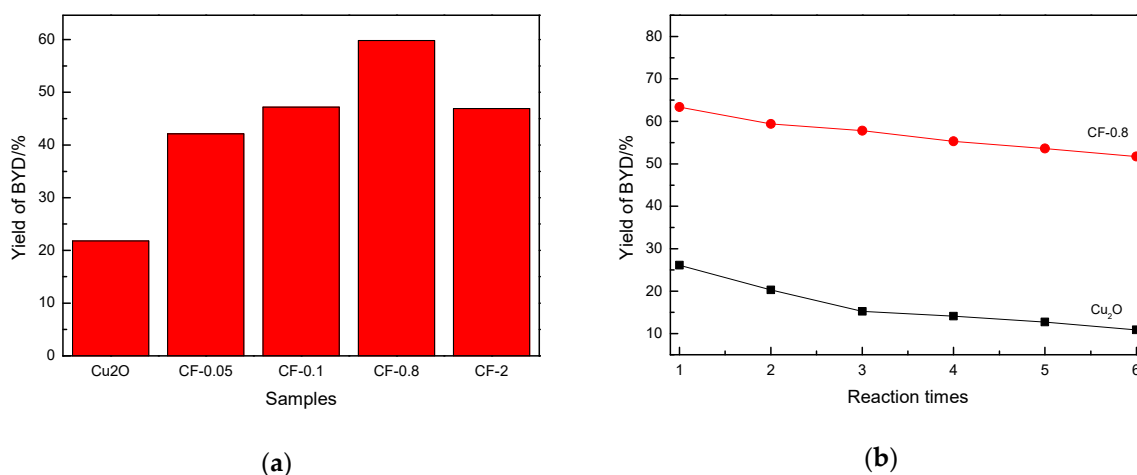

Figure 8. Catalytic performances of Cu_2O and Cu_xO-Fe_yO_z.

4. Conclusions

A series of Cu_xO-Fe_yO_z nanocatalysts with different Fe/Cu ratios were prepared by the oxidation–reduction reaction between Cu^{2+} and Fe^{3+} by and using Cu_2O and $Fe(NO_3)_3$ as raw materials. The introduced Fe^{3+} reacted with Cu_2O to form Cu^{2+} and transformed itself into Fe^{2+} so that Cu_xO-Fe_yO_z nanocomposite particles preferentially formed at the edges, arrises, and corners of the Cu_2O crystal. As the Fe/Cu ratio increased, the content of Cu_xO-Fe_yO_z increased, and Cu_xO-Fe_yO_z gradually spread to the exposed crystal surface of Cu_2O. Moreover, Cu^{2+}/Cu^+, Fe^{2+}/Fe^{3+}, and Fe/Cu ratios increased in Cu_xO-Fe_yO_z. When the Fe/Cu ratio was 0.8, a core–shell structure of the $Cu_2O@Cu_xO$-Fe_yO_z catalyst formed, with an inner core of Cu_2O and an outer layer of Cu_xO-Fe_yO_z. When the Fe/Cu ratio continued to be increased, the crystal structure of Cu_2O disappeared, forming a Cu_xO-Fe_yO_z nanocomposite catalyst that was internally and externally uniform. In the catalyst with a Fe/Cu ratio of 0.8, a heterogeneous structure formed between Cu_xO and Fe_yO_z, and the coexistence of Cu^{2+}, Cu^+, Fe^{2+}, and Fe^{3+} maintained the stability of Cu^+ in a reducing atmosphere of formaldehyde ethynylation and inhibited the excess reduction of Cu^+ to metal Cu species. Meanwhile, the Cu_xO-Fe_yO_z shell with the rough, amorphous structure exhibited a high physical specific surface. Under the combined action of both sides, the Cu^+ active site exposed to the outer surface was the most prominent and showed the best ethynylation activity.

spectra of Cu_2O and Cu_xO-Fe_yO_z catalysts, Figure S2: Structural and textural data of the Cu_2O and Cu_xO-Fe_yO_z catalysts, Table S2: Structural and textural data for the Cu_2O and Cu_xO-Fe_yO_z catalysts, Figure S3: XRD patterns of used the Cu_2O and Cu_xO-Fe_yO_z catalysts, Table S3: Catalytic activity of different catalysts, Figure S4: Cu LMM XAES spectra of the Cu_2O and Cu_xO-Fe_yO_z catalysts used after reaction.

Author Contributions: The idea was conceived by H.L. and L.B. L.B. performed the experiments and drafted the paper under the supervision of Y.Z. and H.L. Z.N. helped to collect and analyze characterization data. The manuscript was revised through the comments of all authors. All authors have given approval for the final version of the manuscript.

Conflicts of Interest: The authors declare no conflicts of interest.

References

1. Tanielyan, S.; Schmidt, S.; Marin, N.; Alvez, G.; Augustine, R. Selective hydrogenation of 2-butyne-1,4-diol to 1,4-butanediol over particulate Raney® nickel catalysts. *Top. Catal.* **2010**, *53*, 1145–1149. [CrossRef]

2. Nadgeri, J.M.; Telkar, M.M.; Rode, C.V. Hydrogenation activity and selectivity behavior of supported palladium nanoparticles. *Catal. Commun.* **2008**, *9*, 441–446. [CrossRef]

3. Trotus, I.T.; Zimmermann, T.; Schüth, F. Catalytic reactions of acetylene: A feedstock for the chemical industry revisited. *Chem. Rev.* **2014**, *114*, 1761–1782. [CrossRef] [PubMed]

4. Li, H.; Zhao, Y.; Gao, C.; Wang, Y.; Sun, Z.; Liang, X. Study on deactivation of Ni/Al_2O_3 catalyst for liquid phase hydrogenation of crude 1,4-butanediol aqueous solution. *Chem. Eng. J.* **2012**, *181–182*, 501–507. [CrossRef]

5. Zhao, F.Y.; Ikushima, Y.; Arai, M. Hydrogenation of 2-butyne-1,4-diol in supercritical carbon dioxide promoted by stainless steel reactor wall. *Catal. Today* **2004**, *93–95*, 439–443. [CrossRef]

6. Zhang, Q.; Zhang, Y.; Li, H.; Gao, C.; Zhao, Y. Heterogeneous CaO-ZrO_2 acid-base bifunctional catalysts for vapor-phase selective dehydration of 1,4-butanediol to 3-buten-1-ol. *Appl. Catal. A Gen.* **2013**, *466*, 233–239. [CrossRef]

7. Li, H.T.; Ban, L.J.; Wang, Z.P.; Meng, P.F.; Zhang, Y.; Wu, R.F.; Zhao, Y.X. Regulation of Cu species in CuO/SiO_2 and its structural evolution in ethynylation reaction. *Nanomaterials* **2019**, *9*, 842. [CrossRef]

8. Yang, G.F.; Li, H.T.; Zhang, H.X.; Wang, Z.P.; Liu, L.L.; Zhao, Y.X. Effect of NaOH concentration on structure and catalytic performance of Cu_2O for formaldehyde ethynylation. *J. Mol. Catal.* **2016**, *30*, 540–546.

9. Eugene, V.H.; Pispacaway, N.J. Ethynylation Catalyst and Process for Production Alkynols by Low Pressure Reactions. US 3920759, 18 November 1975.

10. Zak, D.J. Butynediol Production. US 4085151, 18 April 1978.

11. Fremont, J.M. Preparation of Butynediol Using Bismuth Modified Spheroidal Malachite. U.S. Patent 4127,734, 28 November 1978.

12. Haas, T.; Jaeger, B.; Weber, R.; Mitchell, S.F.; King, C.F. New diol process: 1,3-propanediol and 1,4-butanediol. *Appl. Catal. A Gen.* **2005**, *280*, 83–88. [CrossRef]

13. Ma, Z.Q.; Zhang, H.X.; Li, H.T. Preparation of core-shell CuO-Bi_2O_3@meso-SiO_2 catalyst and its catalytic performance for formaldehyde ethynylation. *Ind. Catal. (China)* **2015**, *23*, 344–348.

14. Luo, M.; Li, H.T.; Ma, Z.Q.; Wang, J.J.; Zhao, Y.X. Researches on activation process of CuO-Bi_2O_3/SiO_2-MgO catalyst in formaldehyde ethynylation reaction. *Ind. Catal. (China)* **2014**, *22*, 363–368.

15. Zheng, Y.; Sun, Z.J.; Wang, Y.Z.; Li, H.T.; Wang, S.A.; Luo, M.; Zhao, J.L.; Zhao, Y.X. Preparation of CuO-Bi_2O_3/SiO_2-MgO catalyst and its ethynylation performance. *J. Mol. Catal. (China)* **2012**, *26*, 233–238.

16. Wang, J.J.; Li, H.T.; Ma, Z.Q.; Wang, Z.P.; Guo, J.Y.; Zhao, Y.X. Preparation of magnetic CuO-Bi_2O_3/Fe_3O_4-SiO_2-MgO catalyst and its catalytic performance for formaldehyde ethynylation. *J. Chem. Ind. Eng.* **2015**, *66*, 2098–2104.

17. Wang, Z.P.; Niu, Z.Z.; Hao, Q.A.; Ban, L.J.; Li, H.T.; Zhao, Y.X.; Jiang, Z. Enhancing the ethynylation performance of CuO-Bi$_2$O$_3$ nanocatalysts by tuning Cu-Bi interactions and phase structures. *Catalysts* **2019**, *9*, 35. [CrossRef]

18. Li, H.T.; Niu, Z.Z.; Yang, G.F.; Zhang, H.X.; Wang, Z.P.; Zhao, Y.X. Support effect of Cu$_2$O/TiO$_2$ employed in formaldehyde ethynylation. *J. Chem. Ind. Eng.* **2018**, *69*, 2512–2518.

19. Wang, Z.P.; Ban, L.J.; Meng, P.F.; Li, H.T.; Zhao, Y.X. Ethynylation of Formaldehyde over Binary Cu-Based Catalysts: Study on Synergistic Effect between Cu+ Species and Acid/Base Sites. *Nanomaterials* **2019**, *9*, 1038. [CrossRef] [PubMed]

20. Li, H.T.; Hao, Q.A.; Wang, Z.P.; Ban, L.J.; Meng, P.F. Study on catalytic of CuO-ZnO catalyst prepared by different precipitants. *Ind. Catal. (China)* **2019**, *33*, 124–131.

21. Lakhera, S.K.; Venkataramana, R.; Watts, A.; Anpo, M.; Neppolian, B. Facile synthesis of Fe$_2$O$_3$/Cu$_2$O nanocomposite and its visible light photocatalytic activity for the degradation of cationic dyes. *Res. Chem. Intermed.* **2017**, *43*, 5091–5102. [CrossRef]

22. Jiang, H.; Dai, Y.; Hu, Y.; Chen, W.; Li, C. Nanostructured ternary nanocomposite of rGO/CNTs/MnO$_2$ for high-rate supercapacitors. *ACS Sustain. Chem. Eng.* **2014**, *2*, 70–74. [CrossRef]

23. Pal, J.; Ganguly, M.; Dutta, S.; Mondal, C.; Negishi, Y.; Pal, T. Hierarchical Au-CuO nanocomposite from redox transformation reaction for surface enhanced Raman scattering and clock reaction. *CrystEngComm* **2014**, *16*, 883–893. [CrossRef]

24. Wang, Z.; Luan, D.; Li, C.M.; Zhang, M.; Lei, D.; Yin, X.; Chen, L.; Li, Q.; Wang, Y.; Wang, T. Magnetite/Graphene composites: Microwave irradiation synthesis and enhanced cycling and rate performances for lithium ion batteries. *J. Mater. Chem.* **2010**, *20*, 5538–5543.

25. Zhao, Z.; Liu, J.; Cui, F.; Feng, H.; Zhang, L. One-pot synthesis of tunable Fe$_3$O$_4$–MnO$_2$ core–shell nanoplates and their applications for water purification. *J. Mater. Chem.* **2012**, *22*, 9052–9057. [CrossRef]

26. Choi, Y.; Hong, S.; Liu, L.; Kim, S.K.; Park, S. Galvanically replaced hollow Au–Ag nanospheres: Study of their surface plasmon resonance. *Langmuir* **2012**, *28*, 6670–6676. [CrossRef] [PubMed]

27. Pal, J.; Mondal, C.; Sasmal, A.K.; Ganguly, M.; Negishi, Y.; Pal, T. Account of nitroarene reduction with size- and facet-controlled CuO–MnO$_2$ nanocomposites. *ACS Appl. Mater. Interfaces* **2014**, *6*, 9173–9184. [CrossRef] [PubMed]

28. Liang, Y.; Chen, Z.; Yao, W.; Wang, P.; Yu, S.; Wang, X. Decorating of Ag and CuO on Cu nanoparticles for enhanced high catalytic activity to the degradation of organic pollutants. *Langmuir* **2017**, *33*, 7606–7614. [CrossRef] [PubMed]

29. Kaviyarasan, K.; Anandan, S.; Mangalaraja, R.V.; Sivasankar, T.; Ashokkumar, M. Sonochemical synthesis of Cu$_2$O nanocubes for enhanced chemiluminescence applications. *Ultrason. Sonochem.* **2016**, *29*, 388–393. [CrossRef] [PubMed]

30. Lakheraa, S.K.; Watts, A.; Haffeez, H.Y.; Neppolian, B. Interparticle double charge transfer mechanism of heterojunction α-Fe$_2$O$_3$/Cu$_2$O mixed oxide catalysts and its visible light photocatalytic activity. *Catal. Today* **2018**, *300*, 58–70. [CrossRef]

31. Huang, K. The long wave modes of the Cu$_2$O Lattice. *Zeitschrift für Physik* **1963**, *171*, 213–225. [CrossRef]

32. Dawson, P.; Hargreave, M.M.; Wilkinson, G.R. The dielectric and lattice vibrational spectrum of cuprous oxide. *J. Phys. Chem. Solids* **1973**, *34*, 2201–2208. [CrossRef]

33. Singhal, A.; Pai, M.R.; Rao, R.; Pillai, K.T.; Lieberwirth, I.; Tyagi, A.K. Copper(I) oxide nanocrystals-one step synthesis, characterization, formation mechanism and photocatalytic properties. *Eur. J. Inorg. Chem.* **2013**, *14*, 2640–2651. [CrossRef]

34. Rodriguez, R.D.; Sheremet, E.; Deckert-Gaudig, T.; Chaneac, C.; Hietschold, M.; Deckert, V.; Zahn, D.R. Surface- and tip-enhanced Raman spectroscopy reveals spin-waves in iron oxide nanoparticles. *Nanoscale* **2015**, *7*, 9545–9551. [CrossRef] [PubMed]

35. Bersani, D.; Lottici, P.P.; Montenero, A. A micro-Raman study of iron-titanium oxides obtained by sol-gel synthesis. *J. Mater. Sci.* **2000**, *35*, 4301–4305. [CrossRef]

36. Huang, W.C.; Lyu, L.M.; Yang, Y.C.; Huang, M.H. Synthesis of Cu$_2$O nanocrystals from cubic to rhombic dodecahedral structures and their comparative photocatalytic activity. *J. Am. Chem. Soc.* **2012**, *134*, 1261–1267. [CrossRef] [PubMed]

37. Cheng, L.; Tian, Y.L.; Zhang, J.D. Construction of p-n heterojunction film of Cu_2O/a-Fe_2O_3 for efficiently photoelectrocatalytic degradation of oxytetracycline. *J. Colloid Interface Sci.* **2018**, *526*, 470–479. [CrossRef] [PubMed]

38. Shang, H.H.; Zhang, X.M.; Xu, J.; Han, Y.F. Effects of preparation methods on the activity of CuO/CeO_2 catalysts for CO oxidation. *Front. Chem. Sci. Eng.* **2017**, *11*, 603–612. [CrossRef]

39. Wang, J.C.; Zhang, L.; Fang, W.X.; Ren, J.; Li, Y.Y.; Yao, H.C.; Wang, J.S.; Li, Z.J. Enhanced photoreduction CO_2 activity over direct z-scheme α-Fe_2O_3/Cu_2O heterostructures under visible light lrradiation. *ACS Appl. Mater. Interfaces* **2015**, *7*, 8631–8639. [CrossRef]

40. Wilson, D.; Langell, M.A. XPS analysis of oleylamine/oleic acid capped Fe_3O_4 nanoparticles as a function of temperature. *Appl. Surf. Sci.* **2014**, *303*, 6–13. [CrossRef]

41. Kuo, C.H.; Huang, M.H. Facile synthesis of Cu_2O nanocrystals with systematic shape evolution from cubic to octahedral structures. *J. Phys. Chem. C* **2008**, *112*, 18355–18360. [CrossRef]

42. Ho, J.Y.; Huang, M.H. Synthesis of submicrometer-sized Cu_2O crystals with morphological evolution from cubic to hexapod structures and their comparative photocatalytic activity. *J. Phys. Chem. C* **2009**, *113*, 14159–14164. [CrossRef]

43. Kim, J.Y.; Park, J.C.; Kim, A.; Kim, A.Y.; Lee, H.J.; Song, H.; Park, K.H. Cu_2O nanocube-catalyzed cross-coupling of aryl halides with phenols via ullmann coupling. *Eur. J. Inorg. Chem.* **2009**, *28*, 4219–4223. [CrossRef]

44. Colacino, E.; Villebrun, L.; Martinez, J.; Lamaty, F. PEG3400-Cu_2O-Cs_2CO_3: An efficient and recyclable microwave-enhanced catalytic system for ligand-free ullmann arylation of indole and benzimidazol. *Tetrahedron* **2010**, *66*, 3730–3735. [CrossRef]

45. Kiss, J.; Óvári, L.; Oszkó, A.; Pótári, G.; Tóth, M.; Baán, K.; Erdóhelyi, A. Structure and reactivity of Au-Rh bimetallic clusters on titanate nanowires, nanotubes and TiO_2(110). *Catal. Today* **2012**, *181*, 163–170. [CrossRef]

46. Óvári, L.; Berkó, A.; Balázs, N.; Majzik, Z.; Kiss, J. Formation of Rh-Au Core-Shell Nanoparticles on TiO_2(110) Surface Studied by STM and LEIS. *Langmuir* **2010**, *26*, 2167–2175. [CrossRef]

47. Zhu, H.; Du, M.L.; Wang, Y.; Wang, L.N.; Zou, M.L.; Zhang, M.; Fu, Y.Q. A new strategy for the surface-free-energy-distribution induced selective growth and controlled formation of Cu_2O-Au hierarchical heterostructures with a series of morphological evolutions. *J. Mater. Chem. A* **2013**, *1*, 919–929. [CrossRef]